



Full Text View

[Volume 32, Issue 7 \(July 2002\)](#)

Journal of Physical Oceanography

Article: pp. 2054–2071 | [Abstract](#) | [PDF \(2.81M\)](#)

Eulerian and Eddy-Induced Meridional Overturning Circulations in the Tropics

James C. McWilliams

National Center for Atmospheric Research, Boulder, Colorado, and Department of Atmospheric Sciences and Institute of Geophysics and Planetary Physics, University of California, Los Angeles, Los Angeles, California

Gokhan Danabasoglu

National Center for Atmospheric Research, Boulder, Colorado

(Manuscript received April 5, 2001, in final form October 29, 2001)

DOI: 10.1175/1520-0485(2002)032<2054:EAEIMO>2.0.CO;2

ABSTRACT

Inspired by recent measurements of the eddy-induced Meridional Overturning Circulation in the tropical North Pacific Ocean by Roemmich and Gilson, the authors analyze an oceanic general circulation model for its Eulerian and eddy-induced Meridional Overturning Circulations throughout the Tropics. The model representation for the mesoscale eddy-induced circulation is the parameterization by Gent and McWilliams, and there are also rectified contributions to the time-mean overturning circulation due to seasonal and interannual fluctuations. The eddy-induced circulation is similar in all tropical basins. It has a strength of about 10% of the Eulerian (mainly Ekman) circulation, and its contribution to the meridional heat flux is a similar fraction. The pattern of the meridional streamfunction is one of double cells in the vertical and antisymmetry about the equator. Near the equator there is downwelling above the undercurrent and upwelling below, with the return circulations closed within the upper 250 m and $\pm 5^\circ$ latitude. Away from the equator in each basin, there are overturning cells with flow in the opposite directions to those nearest the equator, which reach deeper into and through the main pycnocline as well as poleward into the subtropics. Similar to the wind-driven Eulerian Meridional Overturning Circulation, the seasonal cycle in the eddy-induced circulation has a magnitude comparable to the time-mean circulation, although for an entirely different dynamical reason associated with seasonal changes in the buoyancy field that are primarily diabatic. There is also a circulation anomaly during the 1997/98 El Niño–Southern Oscillation event that nearly cancels the time-mean, counterrotating, eddy-induced cells nearest the equator and surface. The rather good agreement between the measurements and the model solution gives support to the theory underlying the parameterization of eddy-induced circulation, and it indicates that the associated eddy transport coefficients are larger

Table of Contents:

- [Introduction](#)
- [Model solutions](#)
- [Mean tropical circulation](#)
- [Seasonal and ENSO tropical](#)
- [Meridional heat flux](#)
- [Observational comparison](#)
- [Concluding remarks](#)
- [REFERENCES](#)
- [FIGURES](#)

Options:

- [Create Reference](#)
- [Email this Article](#)
- [Add to MyArchive](#)
- [Search AMS Glossary](#)

Search CrossRef for:

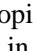
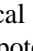
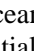
- [Articles Citing This Article](#)

Search Google Scholar for:

- [James C. McWilliams](#)
- [Gokhan Danabasoglu](#)

in the Tropics (i.e., $\sim 2 \times 10^3 \text{ m}^2 \text{ s}^{-1}$) than in middle and high latitudes.

1. Introduction

The upper tropical oceans comprise the core of the global Warm Water Sphere (Wüst 1949). The Tropics are strongly stably stratified in potential density (Fig. 1a ) due primarily to the dominance of solar heating. A secondary influence on the stratification is the freshwater fluxes: evaporation exceeds precipitation away from the equator toward the Subtropics, but this is reversed by heavy precipitation nearer the equator. The strongest tropical currents are zonally oriented (i.e., longitudinal; Fig. 1b ) and driven by the trade winds. Persistent upwelling occurs at the equator, due to the meridional (i.e., latitudinal) divergence of poleward Ekman currents in the surface boundary layer; the closure of this Meridional Overturning Circulation (MOC) by off-equatorial sinking and equatorward flow at depth occurs mainly within the Tropics¹ (Fig. 1c ). Climate equilibrium requires a balancing transport of heat out of the Warm Water Sphere within the ocean, later to be returned to the atmosphere at higher latitudes. Across any bounding isothermal surface enclosing the Warm Water Sphere, this heat transport cannot be accomplished through advection by large-scale currents, nor with sufficient efficiency by isopycnal transport (i.e., directed along a surface of constant potential density) by mesoscale eddies since isotherms and isopycnals are so nearly coincident in this region; hence, the flux is accomplished by the diapycnal fluxes associated primarily with small-scale turbulence (McWilliams et al. 1996). Analogous characterizations can be made for the climate-equilibrium import of freshwater into the Warm Water Sphere, to balance the net surface loss. However, across any bounding latitude line or intercontinental section, these balancing heat and water transports are accomplished primarily by the Ekman MOC, although eddy fluxes could also be important. In this paper we shall adopt the sectional analysis perspective, focusing on the mean and eddy advective transports of mass and heat across sections. We shall make the Boussinesq approximation, common in oceanic general circulation models (OGCMs), that approximates mass flux by volume flux.

The MOC is defined as the zonally averaged northward (meridional) and upward velocity, \mathbf{v} and w [n.b., we denote the eastward (zonal) component by u]. In spherical coordinates, 3D incompressibility is expressed as

$$\nabla \cdot \mathbf{u} \equiv \frac{1}{a \cos \phi} \left[\frac{\partial u}{\partial \lambda} + \frac{\partial (v \cos \phi)}{\partial \phi} \right] + \frac{\partial w}{\partial z} = 0, \quad (1)$$

where (λ, ϕ, z) are spherical coordinates and a is earth's radius. With vanishing normal velocity at solid boundaries, the MOC is 2D nondivergent in the meridional plane, (ϕ, z) , either within a longitudinally bounded basin or an unbounded circumpolar region; namely,

$$\frac{\partial (L_\lambda \langle v \rangle)}{a \partial \phi} + \frac{\partial (L_\lambda \langle w \rangle)}{\partial z} = 0, \quad (2)$$

where $L_\lambda(\phi, z)$ is the zonal basin width and the angle brackets denote a zonal average. Thus, we can represent the MOC in terms of a transport streamfunction, $\Psi(\phi, z)$,

$$\langle v \rangle = -\frac{1}{L_\lambda} \frac{\partial \Psi}{\partial z}, \quad \langle w \rangle = \frac{1}{a L_\lambda} \frac{\partial \Psi}{\partial \phi}. \quad (3)$$

Large-scale Lagrangian transport of mass and material concentrations occurs both by large-scale Eulerian advection and by the averaged flux by (mainly mesoscale) eddies. The eddies cause mixing across large-scale concentration gradients, and they also contribute an eddy-induced mass flux which acts like an additional advecting velocity, \mathbf{u}^* , for material tracers (Gent et al. 1995). In the nearly adiabatic, stably stratified interior of the ocean, the horizontal component of the eddy-induced velocity, $\mathbf{u}_h^* = (u^*, \mathbf{v}^*)$, is defined by

$$\mathbf{u}_h^* = \overline{\mathbf{u}'_h \frac{\partial Z'}{\partial \sigma}} / \frac{\partial \bar{Z}}{\partial \sigma}, \quad (4)$$

where σ is the potential density anomaly relative to 10^3 kg m^{-3} , $Z(\lambda, \phi, \sigma, t)$ is the height of an isopycnal surface, and t is

time. The overbar here denotes an average over the eddies² and the prime denotes a deviation from it. The vertical component, w^* , is defined such that the 3D \mathbf{u}^* is incompressible (i.e., $\nabla \cdot \mathbf{u}^* = 0$). The normal component of \mathbf{u}^* vanishes on solid boundaries because the normal component of \mathbf{u}' vanishes. Thus, an eddy-induced MOC streamfunction, $\Psi^*(\Phi, z)$, may be defined, analogously to Ψ in (3), for the eddy-induced MOC components, $\langle \mathbf{v}^* \rangle$ and $\langle w^* \rangle$,

$$\langle \mathbf{v}^* \rangle = -\frac{1}{L_\lambda} \frac{\partial \Psi^*}{\partial z}, \quad \langle w^* \rangle = \frac{1}{aL_\lambda} \frac{\partial \Psi^*}{\partial \phi}. \quad (5)$$

In most places in the ocean, \mathbf{u}^* is smaller than the large-scale, geostrophic, Eulerian velocity and thus difficult to measure. Nevertheless, its integral effects are believed to be dynamically significant in several situations, notably in the poleward fluxes across the Antarctic Circumpolar Current (Gent and McWilliams 1996), subtropical mass and heat transport in the North Atlantic (Böning et al. 1995), and the seasonal and interannual restratification of the Labrador Sea (Khaliwala and Visbeck 2000)

In an OGCM the computational burden of resolving mesoscale eddies in global equilibrium solutions is quite severe. Consequently, eddy effects are usually parameterized rather than explicitly resolved. Gent and McWilliams (1990) advocate a parameterization for \mathbf{u}^* of the form,

$$\mathbf{u}_h^* = -\frac{\partial}{\partial z} (\kappa_i \mathbf{S}_h), \quad w^* = \nabla_h \cdot (\kappa_i \mathbf{S}_h), \quad (6)$$

for any non-negative eddy transport coefficient, $\kappa_i(\mathbf{x}, t) > 0$, where $\mathbf{S}_h = -\nabla_h \sigma / (\partial \sigma / \partial z)$ is the slope of an isopycnal surface and \mathbf{x} is space. To satisfy the boundary condition on \mathbf{u}^* , we take κ_i smoothly to zero on all boundaries (see appendix B of Large et al. 1997). This parameterization satisfies the criteria of adiabatic integral conservation of material properties and depletion of large-scale available potential energy by the eddies. The use of (6) in coarse-resolution OGCMs yields better distributions and fluxes for large-scale tracer fields than alternative parameterizations that do not respect these criteria (e.g., Danabasoglu et al. 1994; Böning et al. 1995). Subsequently, many analyses of the effects of (6) in coarse-resolution OGCMs have been made (e.g., Nakano and Sugimoto 2002), as have been suggestions for variant or alternative parameterization forms (e.g., Visbeck et al. 1997) and evaluations of \mathbf{u}^* with eddy-resolving OGCMs (e.g., Bryan et al. 1999). Thus far, however, most attention to the eddy-induced circulation and its effects has been outside the Tropics.

A different perspective on the MOC comes from using an isopycnal coordinate instead of a vertical one. We define the isopycnal MOC by its transport streamfunction,

$$\begin{aligned} \Psi_\sigma(\phi, \sigma, t) &= a \cos(\phi) \int d\lambda \int_{-z(\sigma)}^{\eta} dz v \\ &= -a \cos(\phi) \int d\lambda \int_{\sigma}^{\sigma_{\min}} d\sigma v \frac{\partial Z}{\partial \sigma}, \quad (7) \end{aligned}$$

where the zonal integration is made between continental boundaries and η is the oceanic surface elevation. (Analogously, Ψ_σ^* can be defined in terms of \mathbf{v}^* .) Ψ_σ represents the total meridional volume flux above a given σ surface whose height itself varies with space and time. At the extreme (z, σ) values of $(0, \sigma_{\min})$ and $(-H_{\max}, \sigma_{\max})$, Ψ and Ψ_σ are equal and the top-to-bottom difference is the total meridional transport,³ but their distributions in between may differ.

In addition to the difference due to $\sigma(\mathbf{x}, t)$, the time-averaged Ψ and Ψ_σ may differ because the former depends only on the mean Eulerian circulation, \mathbf{v} (i.e., neglecting sea level variations, which our model does through its rigid-lid approximation), while the latter additionally contains a rectified contribution from correlations between \mathbf{v}' and $\partial Z' / \partial \sigma$; that is, it contains the contribution from the eddy-induced circulation as well as the mean circulation. In a numerical model the eddy-induced contribution to Ψ_σ is due only to the transient motions resolved in the solution. It is therefore additive with the additional eddy-induced circulation from the unresolved, or subgrid-scale, motions parameterized in Ψ_σ^* . In the OGCM analyzed here (section 2), the horizontal grid is too coarse to admit mesoscale fluctuations in the solution; therefore, the relevant, resolved, eddy-induced circulation is that due to seasonal and interannual variability, while the mesoscale-induced circulation is wholly parameterized. If the grid were finer, the mesoscale currents would become partly resolved and both the parameterization and analysis would have to be changed accordingly.

There is an extensive literature on the tropical Ekman MOC and its associated meridional heat flux, for both the time mean and seasonal cycle (e.g., [Bryan 1982](#); [Bryden and Brady 1985](#); [Böning and Herrmann 1994](#); [Lee and Marotzke 1997, 1998](#); [Jayne and Marotzke 2000](#); [Carton et al. 2000](#); [Roemmich et al. 2001](#); [Hazeleger et al. 2001](#)). Recently a repeated hydrographic ship track in the tropical North Pacific has allowed a rare observational estimate of the eddy-induced MOC (see [section 6](#) and [Fig. 16](#)) and its associated heat flux across the track ([Roemmich and Gilson 2001](#)). This prompts us to investigate these eddy-induced transports in an OGCM solution with [\(6\)](#) and compare them both to the Eulerian MOC transports in the Tropics and to the observational estimates.

2. Model solutions

We analyze a global OGCM solution forced by a repeated cycle of the estimated wind and buoyancy forcing over the past 42 yr (Doney et al. 2002, manuscript submitted to *J. Climate*, hereafter DYDLM). The model used is the current version of the National Center for Atmospheric Research (NCAR) Climate System Model (CSM) Ocean Model (NCOM; [Gent et al. 1998](#)), which includes [\(6\)](#), its accompanying parameterization for isopycnal tracer diffusion, and a new parameterization of mesoscale-eddy momentum flux with an anisotropic horizontal eddy viscosity where the transverse diffusion coefficient is less than the longitudinal one ([Large et al. 2001](#)). This latter parameterization yields stronger and narrower, and thus more realistic, tropical zonal currents than occur with the conventional isotropic horizontal eddy viscosity on a moderately coarse horizontal grid (here 66 km in the meridional direction near the equator and increasing to 105 km by the poleward edges of the Tropics). For [\(6\)](#) we use a spatially uniform value of $\kappa_i = 0.8 \times 10^3 \text{ m}^2 \text{ s}^{-1}$ outside of the (diabatic) surface boundary layer—lacking, as yet, confidence in a prescription for how κ_i should vary in space and time, as it undoubtedly does (cf., [Visbeck et al. 1997](#)). This value is on the same order as empirical float dispersion estimates (e.g., [Krauss and Böning 1987](#); [Sundermeyer and Price 1998](#); [Bauer et al. 1998](#)), which do show some degree of geographical variation, albeit still largely unsurveyed. The OGCM value for κ_i is chosen primarily to make the Antarctic Circumpolar Current transport approximately the same as observed, based on its dominant role in the horizontal heat and vertical momentum fluxes there. However, as we shall see in [section 6](#), there are good reasons to believe that κ_i has a larger value in the Tropics than in the extratropics.

A comparison with \mathbf{u}^* in an alternative OGCM solution shows only a weak sensitivity to the model grid resolution when the grid resolution is coarsened by 50%. This indicates that the spatial structure of $\sigma(\mathbf{x})$ is well resolved in the Tropics in the present solutions and that the value of κ_i is not constrained by the model grid size; that is, it represents a physically determined process rather than is merely controlling computationally generated noise. In another OGCM solution where κ_i is increased by 50%, the tropical eddy-induced MOC increases by almost the same amount in magnitude while changing little in shape. This indicates that the structure of $\sigma(\mathbf{x})$ in the Tropics is not controlled in a primary way by the value of κ_i although the magnitude of \mathbf{u}^* is. Elsewhere $\sigma(\mathbf{x})$ is more strongly influenced by the value of κ_i ([Danabasoglu and McWilliams 1995](#)).

We shall focus the analysis here on the Tropics and the time period 1 October 1991–30 September 1999, to match the measurements in [Roemmich and Gilson \(2001\)](#). Our analyses are only of monthly averages from the solution that exhibits no significant variability on shorter timescales. Since this analysis period comes near the end of the repeated 42-yr forcing cycle, the model solution does not suffer importantly from our ignorance of an appropriate initial condition at the beginning of the cycle nor from disequilibrium in the upper ocean (DYDLM).

3. Mean tropical circulation

Several familiar features of the global, time-mean tropical circulation are shown in [Fig. 1](#). The mean potential density stratification, $\overline{\sigma}(\Phi, z)$ ([Fig. 1a](#)), has a shallow pycnocline which is sharpest near the equator. The zonal current, $\langle \overline{u} \rangle(\Phi, z)$ ([Fig. 1b](#)), is strongest in and above the pycnocline; it has a westward Equatorial Current at the surface, eastward Equatorial Undercurrent (EUC) in the pycnocline, eastward Equatorial Countercurrents between $|\Phi| \approx 5 - 10^\circ$ (n.b., only subsurface in the Southern Hemisphere), and westward Trade Wind Drift Currents⁴ poleward of $|\Phi| \approx 10^\circ$. The time-mean Eulerian MOC, $\Psi(\Phi, z)$ ([Fig. 1c](#)), is dominated in the upper ocean by the Ekman cells, with the upward and poleward branches confined to narrow regions near the equator and within the surface boundary layer, respectively. There is substantial hemispheric asymmetry, most evident below the pycnocline, due to the global thermohaline circulation that flows northward throughout the upper 1 km of the ocean in the Atlantic. All of these features are evident from measurements, though measurements are essentially never abundant enough to support the zonal averages shown here. Extensive comparisons between the model solution and tropical measurements are in [Large et al. \(2001\)](#).

The eddy-induced MOC, $\Psi^*(\Phi, z)$ ([Fig. 1d](#)), has a more complicated structure in the meridional plane than Ψ . It is approximately antisymmetric about the equator (as is the Eulerian MOC), due to the even symmetry of the density field

[n.b., (6) for their relationship]. In each hemisphere there are double cells both in the vertical and with latitude. The cells nearest the equator are confined to within $|\phi| = 5^\circ$. They have equatorial downwelling above the EUC and upwelling below it, as a consequence of the bulge in isopycnals⁵ that results from geostrophic balance for $\langle \bar{u} \rangle$. The advective effect of this circulation on σ is to compress the bulge and thus to weaken the geostrophic vertical shear and thereby to expand the depth range of the EUC. The eddy-induced MOC cells away from the equator circulate in the opposite sense, with near-surface downwelling and pycnocline upwelling within and poleward of the Equatorial Countercurrents. These cells are associated with the meridional spreading of the pycnocline towards the subtropics and the associated outcropping edges of the tropical warm-water pool. Notice that the eddy-induced MOC is about an order of magnitude weaker than the Eulerian MOC.⁶ Because of this disparity in magnitude and the lack of anticorrelation between the patterns of Ψ and Ψ^* , we can infer that the causes and effects of the tropical MOC are wholly unlike the eddy-induced MOC cancellation of the Antarctic Circumpolar Eulerian Deacon Cell MOC (Danabasoglu et al. 1994; Gent and McWilliams 1996). The Ψ^* structure here is controlled by the shape of $\bar{\sigma}$ in the upper ocean, which is a consequence of the local wind and buoyancy forcings in the Tropics. In all instances these currents, by their definition in (6), are acting to flatten the geostrophically tilted isopycnal surfaces and thus diminish the available potential energy of the mean circulation.

In Figs. 1e,f are shown the isopycnal MOC counterparts, Ψ_σ and Ψ_σ^* , of Figs. 1c,d. There is, of course, a somewhat complex stretching transformation, $z \leftrightarrow \sigma$, between these counterparts, but that aside they exhibit remarkable similarities. With one notable exception, the significant extrema in Fig. 1c are matched with those in Fig. 1e with roughly similar amplitudes, and ditto for Figs. 1d and 1f. The notable exception is the shallow equatorial recirculation enhancements of the broad Ekman MOC cells in Ψ (i.e., centered at ~ 50 m depth and $\pm 2^\circ$ latitude) but absent in Ψ_σ . Note also that there are opposing circulations to these local Eulerian recirculations in Ψ^* and Ψ_σ^* , though of somewhat weaker magnitude. Hazeleger et al. (2001) also show these enhanced recirculations in Ψ , but not Ψ_σ , in an eddy-resolving OGCM solution and attribute them to an eddy-induced circulation associated with the seasonal cycle and tropical instability waves (TIWs). Our coarser-grid OGCM solution lacks resolved TIW variability but still manifests the enhancements through the parameterization (6), albeit with substantially weaker amplitude than Hazeleger et al. (2001). This is the first of several indications we shall see that (6) is behaving qualitatively correctly in the Tropics but that its coefficient, κ_i , is too small in this region.

We investigate the rectified contributions to Ψ_σ by large-scale, low-frequency fluctuations (i.e., seasonal and interannual) by the decomposition described in the caption of Fig. 2. The contribution from the time-mean circulation (Fig. 2a) is clearly dominant, because of its similarity to Fig. 1e. However, there are non-negligible contributions from the mean-seasonal cycle (Fig. 2b), which mostly shows a spatial shifting of the Ψ_σ pattern at the upper, off-equatorial edges of the Ekman MOC cells; some overall weakening of these cells (especially in the Northern Hemisphere); and some local recirculations in the neighborhood of the EUC. The contribution from interannual variations (Fig. 2c) is even weaker and is largely confined to the EUC region; we shall see in section 4 and Fig. 13 that its spatial pattern is associated with El Niño–Southern Oscillation (ENSO).

In Fig. 3 we show the spatial structure underlying the zonally averaged MOC by examining $\mathbf{v}^*(\lambda, \phi)$ and $\bar{w}^*(\lambda, \phi)$ in horizontal planes at depths that intersect the primary overturning cells in Ψ^* (cf., Fig. 1d). Although there are evident zonal variations, they represent only modest deviations from the zonal averages: the eddy-induced circulation is strongest in the Atlantic near the western boundary, in the central Pacific, and in the eastern Indian near the Indonesian Throughflow. The cells nearest the equator are stronger in the Pacific and Atlantic Oceans than in the Indian, as is also true for the time-mean EUC in these basins (Large et al. 2001). The off-equatorial cells are qualitatively similar in all the basins, excluding the North Indian, which is zonally blocked by the Indian subcontinent in the relevant latitude range. A further indication of the similarity among the basins comes from the vertical profiles of $\langle \mathbf{v} \rangle(z)$ (Fig. 4a) and $\langle \mathbf{v}^* \rangle(z)$ (Fig. 4b) in the latitude range, $|\phi| = 15^\circ - 20^\circ$, chosen to intersect the off-equatorial MOC cells in Fig. 1 and to coincide, approximately, with the ship track of repeated hydrographic measurements (section 6). In this latitude range both types of velocity have poleward flow above the pycnocline and equatorward flow within it. For $\langle \mathbf{v}^* \rangle(z)$ there is also a weak poleward flow at depth, whose transport (i.e., integral over depth) is substantial because its vertical extent is large (Fig. 1d). The velocity profiles in the different basins agree to within about a factor of 2, and the eddy-induced flow is about an order of magnitude weaker than the Eulerian flow. The flows in the South Atlantic are somewhat weaker than those in the other basins, though still generally similar in shape, partly because the thermohaline circulation is strong and equatorward in the upper ocean there and alters the usual structure of wind- and buoyancy-driven tropical currents. Similar conclusions could be drawn about the meridional velocity profiles of the isopycnal MOC (cf., the similarities between Figs. 1c,d and 1e,f).

4. Seasonal and ENSO tropical overturning circulations

It is well known that the Eulerian MOC (and its associated meridional heat transport) have a large seasonal variability in the Tropics—even somewhat stronger in the seasonal extreme differences than the time-mean MOC—as a consequence of

seasonal wind, hence Ekman transport, changes (Bryan 1982; Böning and Herrmann 1994; Lee and Marotzke 1998). The strength of the seasonal MOC in the Tropics in different model solutions is significantly different because of uncertainties in the wind climatology.

This seasonal circulation anomaly is shown for the Eulerian MOC in our solution in Figs. 5–6. The seasonal pattern is one of a cross-equatorial, full-depth cell that is closed within $|\Phi| \leq 20^\circ$, approximately as predicted from the Ekman transport (Fig. 5). Its seasonal extremes occur during the summer [months June–August (JJA)] and winter [December–February (DJF)], with surface flow into the winter hemisphere. The transport is larger in the wider Indo–Pacific Ocean than in the narrower Atlantic, by about a factor of 4 (Fig. 6). The seasonal cell in the Atlantic is least equatorially symmetric, with stronger flow in the Northern Hemisphere. Again, there is considerable similarity between $\Delta\Psi$ and $\Delta\Psi_\sigma$ (not shown).

The same relative magnitude of seasonal variability is true for the eddy-induced MOC, although now because of changes in the seasonal buoyancy flux [see (8) and Fig. 12 below]. The seasonal-anomaly circulation is shown in Figs. 7–11. The anomaly magnitude is much weaker near the equator than it is poleward of $|\Phi| = 10^\circ$, where it mainly has a single $\Psi^*(\Phi)$ cell in the vertical confined to the upper 100 m in depth and roughly even symmetric about the equator (Fig. 7). Its seasonal timing is delayed relative to the Eulerian MOC, with the extremes in the summer/fall [months August–October (ASO)] and winter/spring [February–April (FMA)] (Fig. 10), because the timing of the seasonal thermal extremes lags those in the winds. The spatial pattern of the seasonal Ψ^* is similar in all basins, with similar magnitudes for the $\langle \mathbf{v}^* \rangle(z)$ profiles and a larger transport in the wider Indo–Pacific Ocean than in the narrower Atlantic (Figs. 8 and 11). The seasonal Ψ^* anomaly is weakest in the South Atlantic, as is also true for Ψ . The associated seasonal pattern in $\langle \sigma \rangle(\Phi, z)$ occurs as a result of the off-equatorial heating in the summer/fall hemisphere (Fig. 9) that implies an equatorward surface flow and poleward subsurface flow in \mathbf{v}^* by (6). The seasonal surface heat flux anomaly acts to meridionally shift the outcropping boundaries of the tropical warm pool away from the cooling hemisphere, so the eddy-induced circulation anomaly arises to advectively oppose this shift. Figure 8 also includes a plot of $\Delta\Psi_\sigma^*$ (upper right). There is some pattern similarity with $\Delta\Psi^*$ (upper left), accounting for the $z \leftrightarrow \sigma$ transformation, but the amplitude of the isopycnal seasonal cycle is very much weaker by almost an order of magnitude. This is because the surface buoyancy flux anomalies cause density anomalies (as shown below) that largely carry the eddy-induced overturning circulation anomalies with them in their seasonal cycle.

We show in Fig. 12 that the seasonal buoyancy flux anomaly is the principal cause of the σ (hence Ψ^*) anomalies by evaluating the terms in the approximate upper ocean, zonally averaged, density balance,

$$\frac{1}{h} \int_{-h}^0 dz \left\langle \frac{\partial \sigma}{\partial t} \right\rangle(\phi, z, t) \approx -\frac{1}{h} \left\langle \frac{\alpha}{C_p} \delta Q_{a-s} \right\rangle(\phi, t), \quad (8)$$

where α is the thermal expansion coefficient, C_p is the heat capacity, δQ_{a-s} is the seasonal air–sea heat flux anomaly, and $h = 50$ m is the thickness of the layer in which most of the seasonal change occurs (Fig. 9). This balance is satisfied to within $\mathcal{O}(10\%)$ at all tropical latitudes and phases of the seasonal cycle. Thus, seasonal changes in σ due to wind anomalies (via advection by Ekman circulation) are of only secondary importance.

The strongest interannual variability in Ψ^* in our solution occurs in association with an ENSO event. In Fig. 13 we show the annual anomaly in the Pacific during May 1997–April 1998, which is the peak period for the event in the index time series defined by Trenberth (1997). The ENSO circulation anomalies (Figs. 13a,b,d,e) are largely confined to the upper 100 m within 5° of the equator. Their pattern is an antisymmetric pair of cells in Ψ and $\Psi^*(\Phi, z)$, more clearly for Ψ^* . For the latter the shape is similar to the time-mean Ψ^* (Fig. 1d) in this region, but with the opposite sign and with a magnitude that nearly cancels out these cells in the Pacific during ENSO. The cause of this is the near-surface, equatorial anomaly in $\langle \sigma \rangle$ (Fig. 13c) that occurs because of the positive oceanic heat-content anomaly and consequent heat flux to the atmosphere during ENSO (Trenberth et al. 2002). The isopycnal streamfunction anomalies (Figs. 13d,e) are structurally similar to the Ψ and Ψ^* anomalies (Figs. 13a,b) but somewhat weaker in a spatially nonuniform way. Thus, the spatial correlations between σ and (\mathbf{v} , \mathbf{v}^*) anomalies in ENSO are nontrivial but not as strong as they are in the mean-seasonal cycle (cf., Fig. 8).

5. Meridional heat flux

The Eulerian MOC is the primary agent of meridional heat and water fluxes in the Tropics. We define the advective heat flux across a line of latitude by

$$Q(\phi) = \rho_o \int L_\lambda \langle C_p v \theta \rangle dz, \quad (9)$$

where ρ_o is the mean density and θ is the potential temperature. An analogous heat flux by the eddy-induced advection is defined by

$$Q^*(\phi) = \rho_o \int L_\lambda \langle C_p v^* \theta \rangle dz. \quad (10)$$

These fluxes are insensitive to the mean value for temperature since the depth-integrated mass flux is zero in the rigid-lid, Boussinesq approximations for the OGCM.

The time-mean heat fluxes are shown in [Fig. 14](#). In $\overline{Q}(\phi)$ the flux is everywhere northward in the Atlantic, due to the dominant influence of the thermohaline circulation there, and it is poleward in both hemispheres in the Indo-Pacific. The global total is mostly poleward. The Atlantic contribution is dominant in the Northern Hemisphere, and the Indo-Pacific one is dominant in the Southern Hemisphere. Overall these OGCM heat fluxes are on the order of 1 PW and they are roughly consistent with observational estimates (see [Large et al. 1997](#)), although on average the model estimates are somewhat smaller, especially in the North Indo-Pacific ([Trenberth and Caron 2001](#)). In $\overline{Q}^*(\phi)$ the near-equatorial magnitudes are quite small, in part because the contributions from the counterrotating cells in [Figs. 1d,f](#) tend to cancel in a vertical integral, but they exceed 0.1 PW in the region of the Trade Wind Drift Currents and around the outcropping edges of the tropical warm pool ([Fig. 1b](#)). The eddy-induced flux there is equatorward (i.e., mostly in opposition to the Eulerian flux), although there is a weaker poleward flux in the North Equatorial Countercurrent. Here $\overline{Q}^*(\phi)$ is substantially larger in the Indo-Pacific than in the Atlantic. The meridional heat flux by mesoscale-eddy mixing along isopycnal surfaces is relatively small compared to the eddy-induced advection in the Tropics, because of the approximate coincidence of isopycnals and isotherms ([McWilliams et al. 1996](#)); if it were included in [Fig. 14](#), its effect would be barely discernible.

The seasonal-extreme, heat-flux difference in [Fig. 15](#) is even larger than the mean flux for the Eulerian circulation. It carries heat across the equator from the summer/heating to the winter/cooling hemisphere (i.e., in the same sense as the upper-ocean, seasonal, MOC currents; [Fig. 5](#)). In contrast, the eddy-induced, seasonal-extreme, heat-flux difference⁷ is somewhat weaker than \overline{Q}^* . The flux is mostly directed toward the summer/heating hemisphere, in opposition to the Eulerian flux. It is strongest at the latitudes in between the Equatorial Countercurrents and the Trade Wind Drift Currents ([Fig. 1b](#)) near the equatorward edge of the seasonal-extreme circulation difference ([Fig. 8](#)).

6. Observational comparison in the tropical North Pacific

The eddy-induced transport velocity is difficult to measure because of its weakness compared to local Eulerian currents and its spatial and/or temporal averaging requirements. An estimate of the eddy-induced MOC in the tropical North Pacific has recently been made using the section-normal component of geostrophic velocity v_\perp^g , temperature θ , and a constructed salinity S field ([Gilson et al. 1998](#)) in evaluating (4), along the repeated hydrographic line from San Francisco to Taiwan or Hong Kong via Honolulu at an average latitude of about 20°N ([Roemmich and Gilson 2001](#)). This in turn is used to estimate the eddy-induced mass transport across the section in temperature classes as follows:

$$\begin{aligned} \overline{T}_\perp^* &= \int \overline{T}_\perp^*(\theta) d\theta, \\ \overline{T}_\perp^*(\theta) &= \int_\theta \left(\overline{v}_\perp^* \frac{\partial \overline{Z}}{\partial \theta} \right) dx_\parallel, \end{aligned} \quad (11)$$

where x_\parallel is the along-track coordinate.⁸ The observational estimate for \overline{T}_\perp^* is shown in [Fig. 16d](#), along with the same quantity evaluated from the OGCM solution in [Figs. 16b,c](#).⁹ The modeled and observed $\overline{T}_\perp^*(\theta)$ are quite similar in their vertical structure, apart from greater variability with θ for the measurements which we interpret as sampling variability associated with the finite number of eddies resolved on the hydrographic track, to which a non-eddy-resolving OGCM is not vulnerable. However, the observed total northward and southward transport magnitudes are larger by about a factor of 2.6 than in the model solution. Given the approximate proportionality of \mathbf{u}^* with κ_i in the model solutions in this region ([section](#)

2), this suggests that the true value of the eddy diffusivity in the upper tropical ocean may be about $2 \times 10^3 \text{ m}^2 \text{ s}^{-1}$ and that the true strength of the eddy-induced MOC may be only about half an order of magnitude smaller than the Eulerian MOC (cf., [Fig. 16a](#)). Recent observational estimates of κ_i from drifter dispersal rates are at least this large in the Tropics ([Bauer et al. 1998](#)), and estimates from the Extratropics are typically rather smaller and of the order of the value used in the primary OGCM solution here (e.g., [Krauss and Böning 1987](#); [Sundermeyer and Price 1998](#)).

We have not yet calculated an alternative global OGCM solution with a spatially variable κ_i , pending further evidence about what the true spatial variation is. Nevertheless, a simple rationalization of the contrast between the Tropics and extratropics can be made using a mixing-length estimate,

$$\kappa_i \sim V' L', \quad (12)$$

where V' and L' are characteristic values for the eddy horizontal velocity and length scales: given that V' values are not smaller in the Tropics and that L' values are larger (in part because the deformation radius is larger; see [Stammer 1998](#)), then κ_i is expected to be larger in the Tropics. A more quantitatively explicit estimate from baroclinic-instability theory ([Visbeck et al. 1997](#)) also gives larger values for κ_i in the Tropics when evaluated with an OGCM solution ([Bryan et al. 1999](#)).

The vertical structure of $\bar{T}'_{\perp}(\theta)$ in [Figs. 16b,c,d](#) is close to what we have seen in the time-mean, eddy-induced MOC profiles in all basins ([Fig. 4b](#)): poleward flow in the surface layer, equatorward flow in the upper pycnocline, and weak or poleward flow in the lower pycnocline. For a comparison we also plot the time-mean, Eulerian, section-normal transport in [Fig. 16a](#). It too has the characteristics previously shown for the MOC: it is much stronger than the eddy-induced MOC, its surface (Ekman)-layer flow is poleward, and the equatorward return flow extends throughout the pycnocline and deeper.

We can make a further, partly independent, observational comparison for this repeated hydrography line, namely, the profile of total, time-mean, normal volume flux in temperature classes ([Fig. 17](#)). For the OGCM solution, this is the sum of the resolved-flow flux ([Fig. 16a](#)) and the parameterized eddy-induced flux ([Fig. 16b](#)), and for the eddy-resolving observations it is the time- and along-track average of the resolved flux ([Roemmich et al. 2001](#)). To make the comparison as favorable to the model as possible, we amplify the parameterized eddy-induced flux by the same factor of 2.6 that made the eddy-induced transports agree (i.e., [Figs. 16b,c,d](#)); this has the effect of making the eddy-induced contribution to the total flux about 25% as large as the mean Ekman MOC flux (cf., the transport magnitudes in [Figs. 16a and 17a](#)). The observational comparison ([Figs. 17a,b](#)) is rather good in profile shape, but the OGCM magnitude is about 20% smaller than the observed. Given the dominance of the Ekman MOC in these profiles, and its sensitivity to the mean wind forcing which has observational uncertainties in the Tropics of at least this level (e.g., [Trenberth et al. 1990](#)), we believe that no strong conclusions can be drawn about the discrepancies in [Fig. 17](#).

The section-normal, eddy-induced meridional heat flux, Q'_{\perp} , is small in the OGCM solution, consistent with the mean latitude being near a zero in $Q^*(\Phi)$ ([Fig. 14b](#)). Q'_{\perp} is of the opposite sign and not quite so small in [Fig. 9c](#) of [Roemmich and Gilson \(2001\)](#), but we hesitate to make too much of this discrepancy because of the likelihood of the ship track being near a zero-flux line. Also, we hesitate to compare seasonal and interannual variabilities in the solution and measurements, both because, as presently reported, they are not well determined empirically and because our forcing fields do not have interannual variability in shortwave radiation that is likely to be important in the tropics (DYDLM).

7. Concluding remarks

We have shown that the tropical Eulerian and eddy-induced Meridional Overturning Circulations in an OGCM solution each have rather similar structures in all of the major ocean basins. This is true for both the time-mean and the seasonal-anomaly flows. The essential nature of the Eulerian MOC is the wind-driven Ekman current, whose similarity is a consequence of the similarity of the trade winds in all tropical basins. The primary contribution to the time-mean isopycnal MOC is from the time-mean circulation but there are modest, eddy-induced contributions from the mean-seasonal cycle, interannual variability, and mesoscale eddies (here parameterized). The nature of the eddy-induced MOC is the release of potential energy by the eddies from the sloping tropical pycnocline. Its similarity in the basins is due to the similarity of the geostrophically balanced zonal currents and air-sea heat fluxes. The eddy-induced MOC and its associated meridional heat flux are weaker than their Eulerian counterparts, though not negligibly so.

The OGCM result is approximately confirmed by empirical estimates of the time-mean total and eddy-induced MOCs across a repeated hydrographic line in the off-equatorial Tropical North Pacific. However, this comparison indicates that the present specification of the magnitude of the eddy transport coefficient in the models, κ_i , is incomplete by neglecting spatial

variations and that its magnitude in the Tropics needs to be larger than in the extratropics. The limited geographical range of present measurements precludes a more extensive evaluation of the OGCM eddy-induced circulation. In particular, the OGCM result for the near-equatorial MOC associated with the Equatorial Undercurrent and its ENSO fluctuations is as yet largely untested, although comparison with a TIW-resolving OGCM suggests, again, that κ_i is elevated there compared to the extratropics.

Nevertheless, the agreement shown here between the North Pacific measured and OGCM parameterized $\langle \mathbf{u}^* \rangle$ —that is, a close correspondence in shape and not an essential disagreement in magnitude—does provide an important confirmation of our understanding of the role of eddies in the general circulation. To advance further on this topic requires extensive additional measurements and eddy-resolving model studies.

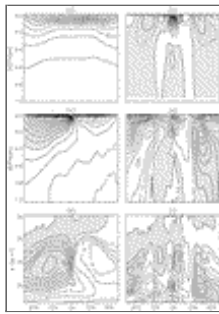
Acknowledgments

We gratefully acknowledge support from the National Science Foundation through Grant OCE 96-18126 and the National Center for Atmospheric Research.

REFERENCES

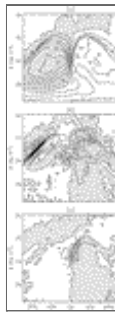
- Bauer S., M. S. Swenson, A. Griffa, A. J. Mariano, and K. Owens, 1998: Eddy-mean flow decomposition and eddy-diffusivity estimates in the tropical Pacific Ocean: 1. Methodology. *J. Geophys. Res.*, **103**, 30855–30871. [Find this article online](#)
- Böning C. W., and P. Herrmann, 1994: Annual cycle of poleward heat transport in the ocean: Results from high-resolution modeling of the North and Equatorial Atlantic. *J. Phys. Oceanogr.*, **24**, 91–107. [Find this article online](#)
- Böning C. W., W. R. Holland, F. O. Bryan, G. Danabasoglu, and J. C. McWilliams, 1995: An overlooked problem in model simulations of the thermohaline circulation and heat transport in the Atlantic Ocean. *J. Climate*, **8**, 515–523. [Find this article online](#)
- Bryan K., 1982: Seasonal variation in meridional overturning and poleward heat transport in the Atlantic and Pacific Oceans: A model study. *J. Mar. Res.*, **40**, 39–53, (Suppl.). [Find this article online](#)
- Bryan K., J. K. Dukowicz, and R. D. Smith, 1999: On the mixing coefficient in the parameterization of bolus velocity. *J. Phys. Oceanogr.*, **29**, 2442–2456. [Find this article online](#)
- Bryden H. L., and E. C. Brady, 1985: Diagnostic model of the three-dimensional circulation in the upper equatorial Pacific Ocean. *J. Phys. Oceanogr.*, **15**, 1255–1273. [Find this article online](#)
- Carton J., J. Wang, and M. Rienecker, 2000: Ocean climate and heat in perspective: An ocean reanalysis project. U.S. WOCE Office, Dept. of Oceanogr., Texas A&M University Rep. 12, 36–39.
- Danabasoglu G., and J. C. McWilliams, 1995: Sensitivity of the global ocean circulation to parameterizations of mesoscale tracer transports. *J. Climate*, **8**, 2967–2987. [Find this article online](#)
- Danabasoglu G., and P. R. Gent, 1994: The role of mesoscale tracer transports in the global ocean circulation. *Science*, **264**, 1123–1126. [Find this article online](#)
- Gent P. R., and J. C. McWilliams, 1990: Isopycnal mixing in ocean circulation models. *J. Phys. Oceanogr.*, **20**, 150–155. [Find this article online](#)
- Gent P. R., 1996: Eliassen–Palm fluxes and the momentum equations in non-eddy-resolving ocean circulation models. *J. Phys. Oceanogr.*, **26**, 2540–2546. [Find this article online](#)
- Gent P. R., J. Willebrand, T. J. McDougall, and J. C. McWilliams, 1995: Parameterizing eddy-induced tracer transports in ocean circulation models. *J. Phys. Oceanogr.*, **25**, 463–474. [Find this article online](#)
- Gent P. R., F. O. Bryan, G. Danabasoglu, S. C. Doney, W. R. Holland, W. G. Large, and J. C. McWilliams, 1998: The NCAR Climate System Model global ocean component. *J. Climate*, **11**, 1287–1306. [Find this article online](#)
- Gilson J., D. Roemmich, B. Cornuelle, and L.-L. Fu, 1998: Relationship of TOPEX/Poseidon altimetric height to steric height and circulation in the North Pacific. *J. Geophys. Res.*, **103**, 27947–27965. [Find this article online](#)
- Hazeleger W., G. P. de Vries, and J. van Oldenborgh, 2001: Do tropical cells ventilate the Indo-Pacific equatorial thermocline? *Geophys. Res. Lett.*, **28**, 1763–1766. [Find this article online](#)

- Jayne S. R., and J. Marotzke, 2000: The dynamics of ocean heat transport variability. *Int. WOCE Newslett.*, **38**, 7–9. [Find this article online](#)
- Khatiwala S., and M. Visbeck, 2000: An estimate of the eddy-induced circulation in the Labrador Sea. *Geophys. Res. Lett.*, **27**, 2277–2280. [Find this article online](#)
- Klinger B. A., and J. Marotzke, 2000: Meridional heat transport by the subtropical cell. *J. Phys. Oceanogr.*, **30**, 696–705. [Find this article online](#)
- Krauss W., and C. Böning, 1987: Lagrangian properties of eddy fields in the northern North Atlantic as deduced from satellite-tracked buoys. *J. Mar. Res.*, **45**, 259–291. [Find this article online](#)
- Large W. G., G. Danabasoglu, S. C. Doney, and J. C. McWilliams, 1997: Sensitivity to surface forcing and boundary layer mixing in a global ocean model: Annual-mean climatology. *J. Phys. Oceanogr.*, **27**, 2418–2447. [Find this article online](#)
- Large W. G., J. C. McWilliams, P. R. Gent, and F. O. Bryan, 2001: Equatorial circulation of a global ocean climate model with anisotropic horizontal viscosity. *J. Phys. Oceanogr.*, **31**, 518–536. [Find this article online](#)
- Lee T., and J. Marotzke, 1997: Inferring meridional mass and heat transports of the Indian Ocean by fitting a general circulation model to climatological data. *J. Geophys. Res.*, **102**, 10585–10602. [Find this article online](#)
- Lee T., 1998: Seasonal cycle of meridional overturning and heat transport of the Indian Ocean. *J. Phys. Oceanogr.*, **28**, 923–943. [Find this article online](#)
- McCreary J., and P. Lu, 1994: Interaction between the subtropical and equatorial ocean circulations: The subtropical cell. *J. Phys. Oceanogr.*, **24**, 466–497. [Find this article online](#)
- McWilliams J. C., G. Danabasoglu, and P. R. Gent, 1996: Tracer budgets in the Warm Water Sphere. *Tellus*, **48A**, 179–192. [Find this article online](#)
- Nakano H., and N. Sugimoto, 2002: Effects of bottom boundary layer parameterization on reproducing deep and bottom waters in a World Ocean model. *J. Phys. Oceanogr.*, **32**, 1209–1227. [Find this article online](#)
- Roemmich D., and J. Gilson, 2001: Eddy transport of heat and thermocline waters in the North Pacific: A key to interannual/decadal climate variability? *J. Phys. Oceanogr.*, **31**, 675–688. [Find this article online](#)
- Roemmich D., B. Cornuelle, and R. Weller, 2001: The mean and time-varying meridional transport of heat at the tropical/subtropical boundary of the North Pacific Ocean. *J. Geophys. Res.*, **106**, 8957–8970. [Find this article online](#)
- Stammer D., 1998: On eddy characteristics, eddy transports, and mean flow properties. *J. Phys. Oceanogr.*, **28**, 727–739. [Find this article online](#)
- Sundermeyer M., and J. Price, 1998: Lateral mixing and the North Atlantic Tracer Release Experiment: Observations and numerical simulations of Lagrangian particles and a passive tracer. *J. Geophys. Res.*, **103**, 21481–21497. [Find this article online](#)
- Trenberth K. E., 1997: The definition of El Niño. *Bull. Amer. Meteor. Soc.*, **78**, 2771–2777. [Find this article online](#)
- Trenberth K. E., and J. M. Caron, 2001: Estimates of meridional atmosphere and ocean heat transports. *J. Climate*, **14**, 3433–3443. [Find this article online](#)
- Trenberth K. E., W. G. Large, and J. G. Olson, 1990: The mean annual cycle in global ocean wind stress. *J. Phys. Oceanogr.*, **20**, 1742–1760. [Find this article online](#)
- Trenberth K. E., D. P. Stepaniak, and J. M. Caron, 2002: Interannual variations in the atmospheric heat budget. *J. Geophys. Res.*, in press.
- Visbeck M., J. Marshall, T. Haine, and M. Spall, 1997: Specification of eddy transfer coefficients in coarse-resolution ocean circulation models. *J. Phys. Oceanogr.*, **27**, 381–402. [Find this article online](#)
- Wüst G., 1949: Über die Zweiteilung der Hydrosphäre. *Dtsch. Hydrogr. Z.*, **2**, 218–225. [Find this article online](#)



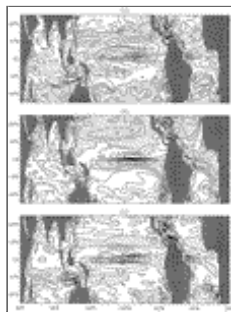
[Click on thumbnail for full-sized image.](#)

FIG. 1. Global, upper-ocean, zonal- and time-mean quantities: (a) potential density, $\bar{\sigma}(\Phi, z)$ [contour interval (CI) = 0.5 kg m^{-3}] (with a surface reference pressure); (b) zonal velocity, $\langle \bar{u} \rangle(\Phi, z)$ (CI = 0.04 m s^{-1} , with dashed lines for $\pm 0.02 \text{ m s}^{-1}$); (c) Eulerian-mean meridional overturning streamfunction, $\Psi(\Phi, z)$ {CI = 4 Sv : $\text{Sv} \equiv 10^6 \text{ m}^3 \text{ s}^{-1}$ }; (d) eddy-induced meridional overturning streamfunction, $\Psi^*(\Phi, z)$ (CI = 0.5 Sv); (e) isopycnal meridional overturning streamfunction, $\Psi_\sigma(\Phi, \sigma)$ (CI = 4 Sv); (f) isopycnal eddy-induced meridional overturning streamfunction, $\Psi^*_\sigma(\Phi, \sigma)$ (CI = 0.5 Sv). Gray shading indicates $\bar{\sigma} \leq 25$ in (a) and negative values in (b)–(f)



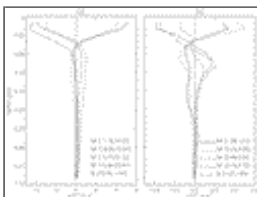
[Click on thumbnail for full-sized image.](#)

FIG. 2. Global, upper-ocean, time-mean, isopycnal meridional overturning streamfunction, $\Psi_\sigma(\Phi, \sigma)$: (a) Ψ_σ calculated with \mathbf{u} and \bar{Z} (i.e., contribution from time-mean flow and isopycnal configuration only) (CI = 4 Sv); (b) difference between Ψ_σ calculated with mean-seasonal \mathbf{u} and Z and (a) (i.e., contribution from mean-seasonal cycle) (CI = 1 Sv); (c) difference between total Ψ_σ in [Fig. 1e](#) and (b) (i.e., contribution from interannual variability) (CI = 1 Sv). The sum of these three panels equals [Fig. 1e](#). Gray shading indicates negative values.



[Click on thumbnail for full-sized image.](#)

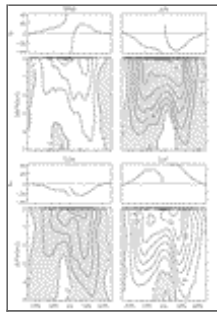
FIG. 3. Time-mean, eddy-induced velocity: (a) $\mathbf{v}^*(\lambda, \Phi)$, averaged over 17–50 m (CI = $0.1 \times 10^{-2} \text{ m s}^{-1}$); (b) $\mathbf{v}^*(\lambda, \Phi)$, averaged over 62–148 m (CI = $0.05 \times 10^{-2} \text{ m s}^{-1}$); and (c) $\bar{w}^*(\lambda, \Phi)$, averaged over 44–71 m (CI = $0.2 \times 10^{-6} \text{ m s}^{-1}$)



[Click on thumbnail for full-sized image.](#)

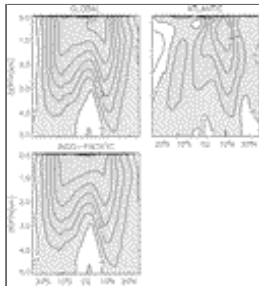
FIG. 4. (a) Zonal-, 15° – 20° -, and Eulerian-time-mean, meridional velocity, $\langle \mathbf{v} \rangle(z)$ (m s^{-1}), in the five basins. Note the stretched depth scale. The inset lists basin labels and their total southward and northward transports (Sv) in the upper ocean ($z \geq -1033 \text{ m}$)

and 15°–20° latitude). (b) The same for eddy-induced velocity, $\langle \mathbf{U}^* \rangle(z)$



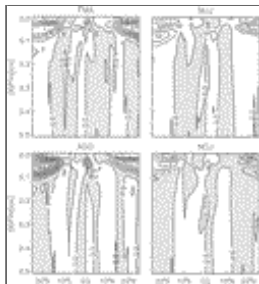
[Click on thumbnail for full-sized image.](#)

FIG. 5. Global, mean-seasonal-anomaly, Eulerian, meridional overturning streamfunction, $\Psi(\phi, z)$ (CI = 4 Sv), for the full depth range, with overlying line curves of seasonal-anomaly Ekman transport, $-L_\lambda(\phi, 0)\langle\delta\tau^{(\lambda)}\rangle/f\rho_o$ [where $\delta\tau^{(\lambda)}(\lambda, \phi)$ is the anomalous zonal wind stress, $f = 2\Omega \sin\phi$ is the Coriolis frequency, Ω is earth's rotation rate, and ρ_o is the mean ocean density]. Gray shading indicates negative anomaly



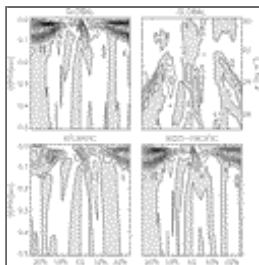
[Click on thumbnail for full-sized image.](#)

FIG. 6. Global, Indo-Pacific, and Atlantic mean-seasonal extremes, $\Delta\Psi(\phi, z)$ (JJA minus DJF) for the full oceanic depth range (CI = 8 Sv, except for the Atlantic seasonal extreme where CI = 2 Sv). Gray shading indicates negative anomaly



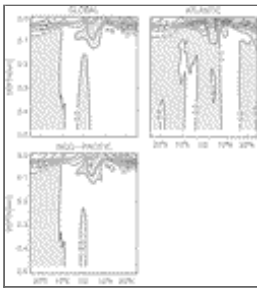
[Click on thumbnail for full-sized image.](#)

FIG. 7. Global, mean-seasonal-anomaly, eddy-induced meridional overturning streamfunction, $\Psi^*(\phi, z)$, in the upper ocean ($z \geq -500$ m) (CI = 0.4 Sv). Gray shading indicates negative anomaly



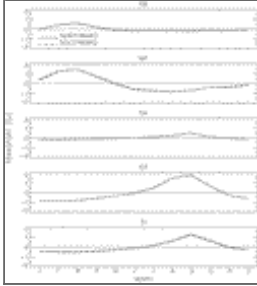
[Click on thumbnail for full-sized image.](#)

FIG. 8. (top left) Global, Atlantic, and Indo-Pacific seasonal extremes, $\Delta\Psi^*(\phi, z)$ (ASO minus FMA), plus (top right) the global, isopycnal counterpart, $\Delta\Psi^*_\sigma(\phi, \sigma)$ (CI = 0.4 Sv, except for the Atlantic mean-seasonal extreme where CI = 0.2 Sv). Gray shading indicates negative anomaly



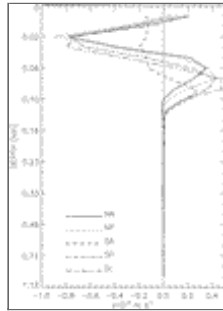
Click on thumbnail for full-sized image.

FIG. 9. Global, Indo-Pacific, and Atlantic seasonal extremes, $\langle \Delta \sigma \rangle(\Phi, z)$ (ASO minus FMA) ($CI = 0.2 \text{ kg m}^{-3}$). Gray shading indicates negative anomaly



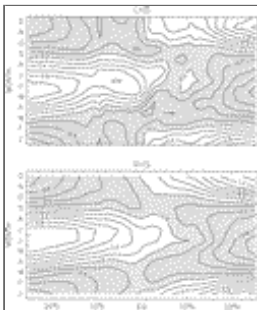
Click on thumbnail for full-sized image.

FIG. 10. Mean-seasonal cycle of total southward and northward, upper-ocean ($z \geq -1033 \text{ m}$), eddy-induced, mass-transport anomaly (Sv) in the five basins and averaged between 15° – 20° latitude



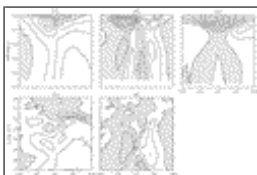
Click on thumbnail for full-sized image.

FIG. 11. Mean-seasonal extreme (ASO minus FMA), $\langle \Delta \mathbf{v}^* \rangle(z)$ (m s^{-1}), averaged between 15° – 20° , with a stretched depth scale



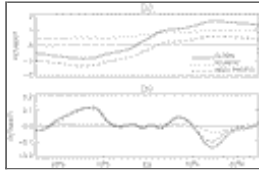
Click on thumbnail for full-sized image.

FIG. 12. Mean-seasonal cycle of the terms in the global zonally averaged, upper-ocean density balance (8): (lhs) content tendency and (rhs) air-sea heat flux ($CI = 0.2 \times 10^{-7} \text{ kg m}^{-3} \text{ s}^{-1}$)



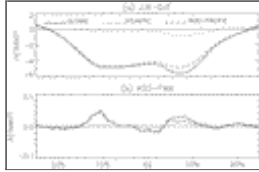
Click on thumbnail for full-sized image.

FIG. 13. Annual-mean anomaly in the Pacific during ENSO (May 1997–Apr 1998): (a) $\Psi(\Phi, z)$ (CI = 2.0 Sv); (b) $\Psi^*(\Phi, z)$ (CI = 0.25 Sv); (c) $\sigma(\Phi, z)$ (CI = 0.1 kg m⁻³); (d) $\Psi_\sigma(\Phi, \sigma)$ (CI = 2.0 Sv); (e) $\Psi_\sigma^*(\Phi, \sigma)$ (CI = 0.25 Sv). Shaded regions indicate negative values



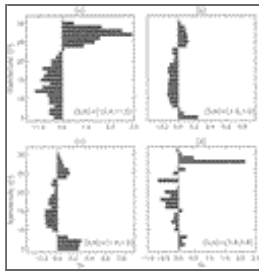
[Click on thumbnail for full-sized image.](#)

FIG. 14. Time-mean heat flux (PW): (a) Eulerian-mean, $\bar{Q}(\Phi)$ and (b) eddy-induced, $\bar{Q}^*(\Phi)$. In each panel are the global total flux and the basin contributions from the Atlantic and Indo–Pacific.



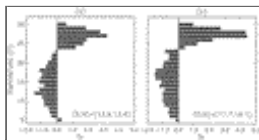
[Click on thumbnail for full-sized image.](#)

FIG. 15. Mean-seasonal extreme heat flux (PW): (a) Eulerian, $\Delta Q(\Phi)$ (JJA minus DJF) and (b) eddy-induced, $\Delta Q^*(\Phi)$ (ASO minus FMA). In each panel are the global total flux and the basin contributions from the Atlantic and Indo–Pacific



[Click on thumbnail for full-sized image.](#)

FIG. 16. Time-mean, normal transport in temperature bins ($\delta\theta = 1^\circ\text{C}$) in the upper ocean ($\theta \geq 5^\circ\text{C}$), averaged in time (8 yr), and integrated along the repeated hydrographic ship track in the tropical North Pacific: (a) modeled Eulerian, $\bar{T}_\perp(\theta)$ (Sv); (b) modeled eddy-induced, $\bar{T}_\perp^*(\theta)$ (Sv); (c) as in (b) except based only on θ [i.e., $S = 35$ psu is used in calculating the density in (6)]; and (d) measured eddy-induced transport, \bar{T}_\perp^* (Sv) (Roemmich and Gilson 2001). Numerical labels indicate total southward and northward transports in the upper ocean. Note the rescaled abscissa between (b)–(c) and (d), by a factor of 2.6, which is about the ratio of the total southward and northward transports in (c) and (d)



[Click on thumbnail for full-sized image.](#)


FIG. 17. Total, time-mean, normal transport in temperature bins ($\delta\theta = 1^\circ\text{C}$) in the upper ocean ($\theta \geq 5^\circ\text{C}$), averaged in time (8 yr), and integrated along the repeated hydrographic ship track in the tropical North Pacific: (a) $\bar{T}_\perp(\theta) + 2.6 \times \bar{T}_\perp^*(\theta)$ (Sv) from the model (note the enhancement of the eddy-induced transport by the same factor as in Fig. 16) and (b) $\bar{T}_\perp(\theta)$ from the eddy-resolving measurements (taken from Fig. 7a of Roemmich et al. 2001)

¹ Oddly enough, these tropical Ekman MOC cells are sometimes referred to as subtropical cells ([McCreary and Lu 1994](#); [Klinger and Marotzke 2000](#)), since part of the downward circulation branch does occur poleward of the Tropics–subtropics boundary at 22.5°.

² In measurements or model solutions that include eddy variability, the average is defined as some type of low-pass, space–time filter. The simplest such choice is a time average, and this is what is used by [Roemmich and Gilson \(2001\)](#) for the eddy-induced mass transport estimated from repeated hydrographic measurements, although they report that an alternative low-pass estimate gives a similar result (see their [section 5](#)). In a model solution without eddies ([section 2](#)), the eddy flux in [\(4\)](#) is formally identified with the model's parameterization form, for example, [\(6\)](#) below. Our opinion is that subtleties in defining averages are not a significant issue for the measurements and calculations in this paper, even though it is easy to imagine that sometimes they would be.

³ This total transport is zero in long-time average for all basins not open to the north. This is true for the global transport and it is approximately true for the Atlantic and Indo–Pacific basins, neglecting Pan-Arctic flow.


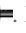
⁴ These are often called the South and North Equatorial Currents.

⁵ This bulge is only faintly evident in [Fig. 1a](#) , but it is much more so in individual meridional sections; for example, see [Bryden and Brady \(1985\)](#).

⁶ But see [section 6](#) for arguments that the tropical eddy-induced MOC is too weak in this OGCM solution by a factor of 2–3.

⁷ The eddy-induced, seasonal-extreme differences, ΔQ^* , are modestly larger, compared to [Fig. 15](#) , when the seasonal phase is shifted forward by a month [i.e., September–October–November (SON) minus March–April–May (MAM)], especially for the northern maximum. This indicates there is a small phase shift between the seasonal mass and heat flux anomalies.

⁸ Note the similarity in information content between \bar{T}^*_{\perp} and Ψ^*_{σ} defined analogously to [\(7\)](#).

⁹ In [Fig. 16b](#) , we calculate \mathbf{v}^*_{\perp} from [\(6\)](#) using the total σ field, but, to assess the S contributions, we alternatively calculate \mathbf{v}^*_{\perp} using only the contribution from θ to σ in [Fig. 16c](#) . In both cases we then multiply by $\partial\bar{z}/\partial\theta$ and zonally integrate along surfaces of constant θ . The similarity of these two results indicates that S variation plays only a minor role here (also stated by [Roemmich et al. 2001](#)).

top ▲



© 2008 American Meteorological Society [Privacy Policy and Disclaimer](#)
Headquarters: 45 Beacon Street Boston, MA 02108-3693
DC Office: 1120 G Street, NW, Suite 800 Washington DC, 20005-3826
amsinfo@ametsoc.org Phone: 617-227-2425 Fax: 617-742-8718
[Allen Press, Inc.](#) assists in the online publication of *AMS* journals.